Preparation of hierarchical SSZ-13 by NH4F etching

Viktoria Babić, Siddardha Koneti, Simona Moldovan, Nikolai Nesterenko, Jean-Pierre Gilson, Valentin Valtchev

Preparation of hierarchical SSZ-13 by NH_4F etching

Viktoria Babić,[1] Siddardha Koneti,[2] Simona Moldovan,[2] Nikolai Nesterenko,[3] Jean-Pierre Gilson,[1] Valentin Valtchev[1,]*

[1]V. Babić, J.-P. Gilson, V. Valtchev

Normandie Univ, ENSICAEN, UNICAEN, CNRS, Laboratoire Catalyse et Spectrochimie, 14000 Caen, France

[2]S. Koneti, S. Moldovan

Institut des Sciences Appliquées de Rouen, Rouen University, Groupe de Physique des Matériaux (GPM), 76801 Rouen, France

[3]N. Nesterenko

Total Research and Technology Feluy (TRTF), Zone Industrielle Feluy C, 7181 Seneffe, Belgium

Corresponding author: *Valentin Valtchev, valtchev@ensicaen.fr

Abstract

NH_4-SSZ-13 was etched with an aqueous solution of 40 *w*/% NH_4F under different time/temperature conditions to obtain hierarchical derivatives. The etched zeolites were characterized by XRD, SEM, N_2 physisorption, ^{29}Si / ^{27}Al / ^{19}F MAS NMR, ICP-AES, and their acidity monitored by *in situ* FTIR spectroscopy using acetonitrile as a probe molecule. The results highlight that the zeolite is very sensitive to high temperature and high liquid-solid ratio treatments leading to substantial crystallinity losses. These two parameters need careful tuning to obtain hierarchical derivatives retaining important characteristics as micropore volume and framework Si/Al ratio. The catalytic activity of the modified SSZ-13 is evaluated in the n-propanol conversion.

Keywords: zeolite, hierarchical, fluoride etching, SSZ-13

1 Introduction

Chabazite, a naturally occurring mineral, was discovered in 1792 by Bosch D'Antic.[1] In 1925, Weigel and Steinhoff studied the adsorption selectivity of dehydrated chabazite.[2] Chabazite is an important member of the small pore, eight-ring zeolites, along with LTA, RHO, ERI, and DDR. The high-silica members of these zeolites have now found widespread application as size-selective adsorbents.[3]

The CHA structure contains large interconnected ellipsoïdal cages (0.67 x 1.1 nm^2), accessible through eight-membered ring windows (0.38 x 0.38 nm^2). The CHA cage ($4^{12}6^2 8^6$) has six octagonal windows (8^6), allowing sorption from all directions[4], and can accommodate fairly large molecules. The structure features of Chabazite explain the unique selectivity to olefins in the MTO process, where the bulky aromatic molecules are prisoned in the cage, and only lower olefins (2-4 carbon atoms) can leave it.[5] In the Al-rich forms of chabazite, the windows are partially obstructed by exchangeable cations.

SSZ-13 is the aluminosilicate analog of CHA-type structure similarly to SAPO-34, later being used commercially along with ZSM-5, in the methanol-to-olefin (MTO) conversion.[6] The SAPO-34 MTO catalyst deactivates fast during operation, and a fluidized bed is required for continuous olefins production.[7] However, SSZ-13 deactivates faster than SAPO-34[8], and extending the lifetime of the SSZ-13 catalyst can be done by shortening the diffusion pathlength on molecules in the microporosity, either by reducing the crystallite size or generating mesopores, *i.e.*, hierarchization.[9] Copper exchanged SSZ-13 has been used as a catalyst for the last decade in NO_x emission control in the ammonia selective catalytic reduction (NH_3-SCR) process.[10]

Often an as-synthesized zeolite does not provide the desired properties, and post-synthesis treatments are required to fine-tune a specific zeolite property.[11] A wide variety of post-synthesis treatments, such as alkaline leaching,[12–14] dealumination by ammonium hexafluorosilicate,[15] nitric acid,[16] and neutron irradiation[17] have been used to prepare hierarchical SSZ-13 with mixed results since they either cause structural collapse or modify acidity.

Traditionally SSZ-13 is synthesized in the presence of N,N,N-trimethyl-1-adamantanammonium hydroxide (TMAdaOH), and the crystals are usually larger than 1 µm.[18] Nanosized SSZ-13 has been successfully synthesized via a one-pot strategy by adding CTAB as a surfactant[6]. Wu et al. prepared mesoporous SSZ-13 using a dual template strategy: a diquaternary-ammonium surfactant ($[C_{22}H_{45}–N^{+}(CH_3)_2–(CH_2)_4–N^{+}(CH_3)_2–C_4H_9Br_2]$ denoted as $C_{22\text{-}4\text{-}4}Br_2$) as sacrificial mesoporogen, along with TMAdaOH.[19,20] The resulting hierarchical catalyst showed increased conversion and improved stability in the MTO reaction. Another study showed that the $C_{22\text{-}4\text{-}4}Br_2$ mesoporogen, along with fluoride anions, could yield hierarchical SSZ-13 with trimodal porosity.[21] Mesoporous SSZ-13 can also be obtained using a mono-quaternary ammonium head group (N-methyl piperidine).[22] Liu et al. explored biphasic/toluene media to generate mesopores in SSZ-13.[23]

Post-synthesis methods, particularly caustic leaching, generate mesopores at the expense of micropore volume. Previous studies focused on the desilication of SSZ-13 showed, despite the introduction of mesopores, no improvement in NH_3-SCR[12] or MTO reaction.[13] Wardani et al. managed to preserve crystallinity and micropore volume of SSZ-13 by leaving the template in the pores during desilication.[14] The activity of SSZ-13 in MTO reaction was improved by neutron irradiation; however, hydrothermal methods of post-synthesis treatment are more practical.[17] Dai et al. employed dealumination by nitric acid to modify the properties of SSZ-13.[16] Their method altered acidity and lowered micropore volume but extended the catalyst lifetime in the ethene-to-propene (ETP) reaction. Haw et al. synthesized mesoporous SSZ-13 using NH_4F-H_2O_2 solutions, retaining the intrinsic zeolite properties.[24] The use of H_2O_2 resulted in the ultra-fast dissolution of SSZ-13 crystals and the formation of a sponge-like structure.

The sole use of NH_4F as an etching agent also allows the preparation of hierarchical zeolites.[25] The ammonium fluoride route to hierarchical zeolites was applied to various low and high silica zeolites to generate mesoporosity while preserving their Si/Al ratio, *i.e.*, acid site concentration. [26] The present study is devoted to the NH_4F etching of SSZ-13 zeolite and comprehensive analysis of its hierarchical derivatives' physicochemical properties.

2 Experimental section

2.1 Post-synthetic treatment

NH_4-SSZ-13 is from ACS Materials (USA). The NH_4F crystals are purchased from Sigma Aldrich, and solutions are freshly made prior to the treatment. The parent sample (NH_4-SSZ-13) is etched with a 40 *wt.* % (mass fraction) ammonium fluoride (NH_4F) solution in a temperature-controlled water bath. The effects of the following parameters are studied: liquid-solid ratio (l/s), temperature, and time.

After NH_4F etching, the solid is recovered by filtration on a cellulose membrane and washed thoroughly with hot water (heated to 90 °C) to remove all leftover products. Samples are dried overnight at 60 °C, carefully ground, and further analyzed.

2.1.1 Sample notation

The sample code employed is CHA-liquid/solid-temperature-time.

Series I: liquid/solid ratio of 8

1 g of NH_4-SSZ-13 is mixed with 8 ml of 40 *w*/% NH_4F at 0, 25, and 50 °C.

T [°C]	Time [min]	
	5	20
0	CHA-8-0-5	CHA-8-0-20
25	CHA-8-25-5	CHA-8-25-20
50	CHA-8-50-5	CHA-8-50-20

Series II: liquid/solid ratio of 20

1 g of NH_4-SSZ-13 is mixed with 20 ml of 40 *w*/% NH_4F at 0, 25, and 50 °C.

T [°C]	Time [min]	
	5	20
0	CHA-20-0-5	CHA-20-0-20
25	CHA-20-25-5	CHA-20-25-20

50	CHA-20-50-5	CHA-20-50-20

Series III: liquid/solid ratio of 100

1 g of NH_4-SSZ-13 is mixed with 100 ml of 40 *w*/% NH_4F 0, 25, and 50 °C.

T [°C]	Time [min]	
	5	20
0	CHA-100-0-5	CHA-100-0-20
25	CHA-100-25-5	CHA-100-25-20
50	CHA-100-50-5	CHA-100-50-20

2.2 Characterization

Powder X-ray diffraction (XRD) patterns are recorded on a Malvern PANalytical X'Pert PRO Diffractometer with CuKα radiation (λ = 1.5418 Å, 45 kV, 40 mA) over a range of 4 - 50° 2θ with a time per step of 0.0167113° s^{-1} using a ¼° divergence slit. Relative crystallinity values are determined from the integrated peak areas between 20 and 32° 2θ [27] and compared with their parent NH_4-SSZ-13. The N_2 physisorption isotherms (-196 °C) are measured on a Micromeritics 3Flex high-resolution surface characterization analyzer. About 100 mg of the sample is outgassed at 300 °C under vacuum by a turbomolecular pump overnight prior to analysis. The isotherms are processed with the MicroActiv analysis program. Micropore volume (V_{micro}) is determined from the porosity distribution obtained from the DFT model (N_2 on oxide surface with cylindrical geometry), and total pore volume (V_{tot}) is determined by the amount of adsorbed nitrogen at p/p_0 = 0.98. Mesopore volume (V_{meso}) is determined from V_{tot} – $V_{micro.}$

Scanning electron microscopy (SEM) pictures are taken on a MIRA TESCAN microscope equipped with a field emission gun. Micrographs are collected under an acceleration voltage of 30 kV. Before measurement, samples are deposited on a sample holder with a conductive adhesive tape and sputtered for 30 s with platinum. Transmission electron microscopy (TEM) micrographss are taken on a JEOL ARM 200 CFeg Analythical TEM at 200 keV using an high angle annular dark field (HAADF) detector under Scanning TEM (STEM) mode. Prior to analysis, the samples are dispersed in ethanol byultrasounds for 20 - 30 minutes before being transferred to a carbon support grid for measurements. EDX (energy dispersive X ray

spectroscopy) is used to map the elements and study samples' composition. Elemental mapping is carried out at 80 kV electron beam in order to limit the electron beam damage. The STEM mode is employed for both imaging and elemental mapping using the DigiScan module from Gatan Digital Micrograph and the AnalysisStation softwares, respectively. The Si and Al contents are determined by inductively coupled plasma atomic emission spectroscopy (ICP-AES) on an AES 5100 VDV ICP from Agilent; all samples are digested in *aqua regia* and HF prior to the analysis.

Solid-state NMR measurements are carried out using 4 mm zirconia rotors and ^{19}F, ^{27}Al, ^{29}Si MAS NMR, spectra are recorded on a Bruker Avance 400 MHz spectrometer (magnetic field of 9.4 T). All experiments are performed with a spinning speed of 14 kHz. The chemical shifts are referenced to a 1 M $Al(NO_3)_3$ aqueous solution, TMS and $CFCl_3$, for ^{27}Al, ^{29}Si, and ^{19}F, respectively. Prior to *in situ* FTIR study, all powders are pressed into self-supporting wafers (2 cm^2) and degassed in-situ at 450 °C for 2 hours under vacuum (0.000133 Pa) inside an IR. The IR spectra (128 scans) are collected on a NICOLET 6700 spectrometer fitted with a DTGS detector with a 4 cm^{-1} optical resolution. All samples are equilibrated for 15 min at room temperature with a pressure of 133 Pa of d_3-acetonitrile (CD_3CN) before recording a spectrum. Spectra are deconvoluted with the OMNIC 8.3.103 software. Quantitative results are obtained using molar absorption coefficients from the literature.[28]: protonated CD_3CN on Brønsted acid sites (2297 cm^{-1}, ε(B) = 2.05 cm μmol^{-1}) and coordinated on Lewis acid sites (2310 cm^{-1}, ε(L) = 3.6 cm μmol^{-1}). Both integrated areas of deconvoluted bands are normalized to a wafer mass of 20 mg.

The dehydration of n-propanol (nPrOH) is an acid-catalyzed test reaction that is used to evaluate the hierarchical derivative performance. It is executed in a downflow fixed-bed reactor operating in the gas phase. A quartz reactor is packed with a mixture of 120 mg inert SiC (particle size 200-300 μm), 30 mg (W, dried basis) catalyst (particle size 200–500 μm), SiC/zeolite ratio 4. The catalysts are activated *in situ* at 450 °C for 4 hours under a dry airflow (50 ml min^{-1}) to remove excess water and generate the H-form of the zeolites, cooled to the reaction temperature (205° C). The N_2 (100 ml min^{-1}) stream is then diverted to a saturator maintained at 5 °C filled with n-propanol and fed to the reactor resulting in a contact time W/F° of 27.2 $kg \cdot mol^{-1} \cdot s$. The online analysis of the products is performed with a gas chromatograph Varian® 3900 gas chromatograph equipped with a WCOT CP-Wax 52 CB 2.0 μm column (35 m x 0.25 mm) and an FID detector at 200 °C. Total coke content is determined by thermogravimetric analysis (TGA). The TGA is carried out in a SETSYS

instrument (SETARAM). Samples are heated in the reconstituted (80 % N_2 + 20 % O_2) airflow to 800 °C.

3 Results

XRD patterns of the parent zeolite and its etched derivatives are plotted in **Figure 1**. Briefly, for better understanding the sample notation, the etched samples are divided into three series. Series I, II and III refer to 8, 20 and 100 liquid-solid ratio used, respectively. CHA-8-x-y, refers to a sample prepared with l/s of 8, x refers to the temperature of preparation, varied form 0 to 50 °C, and y refers to the time of the treatment, varied from 5 to 20 min. Series I zeolites, prepared with a liquid/solid ratio of 8, showed the highest relative crystallinity of 96 - 90 %), with the exception of sample CHA-8-50-20 with 78 %. The latter indicates that higher temperatures promote amorphization. The temperature's impact was more pronounced when an etching solution with a higher liquid/solid ratio was employed. Thus, from the samples from series II with a liquid/solid ratio of 20, only the one prepared at 50 °C (CHA-20-50-20) showed a substantial decrease of crystallinity (77 %). Series III samples analysis further confirmed the impact of temperature. This last series of samples with liquid/solid=100 maintain high crystallinity for the sample prepared at a temperature of 0 and 25 °C. However, the products prepared at 50 °C are examples of substantial amorphization; for instance, the relative crystallinity of CHA-100-50-5 and CHA-100-50-20 was 39 and 9 %, respectively. Thus, the elevated temperatures contribute to the amorphization of the structure. Since all the solutions have the same concentrations of 40 *w*/% NH_4F in water, the liquid/solid ratio modifies the number of fluoride species available for the reaction. Rising overall fluoride content contributes to structural degradation. This effect is the most clearly demonstrated by the series with the highest liquid/sold ratio (series III), which exhibits the highest amorphization level. The amorphization is demonstrated by the decrease in the peak intensity and the appearance of a broad halo in the range of 15-30° 2θ (**Figure 1**).

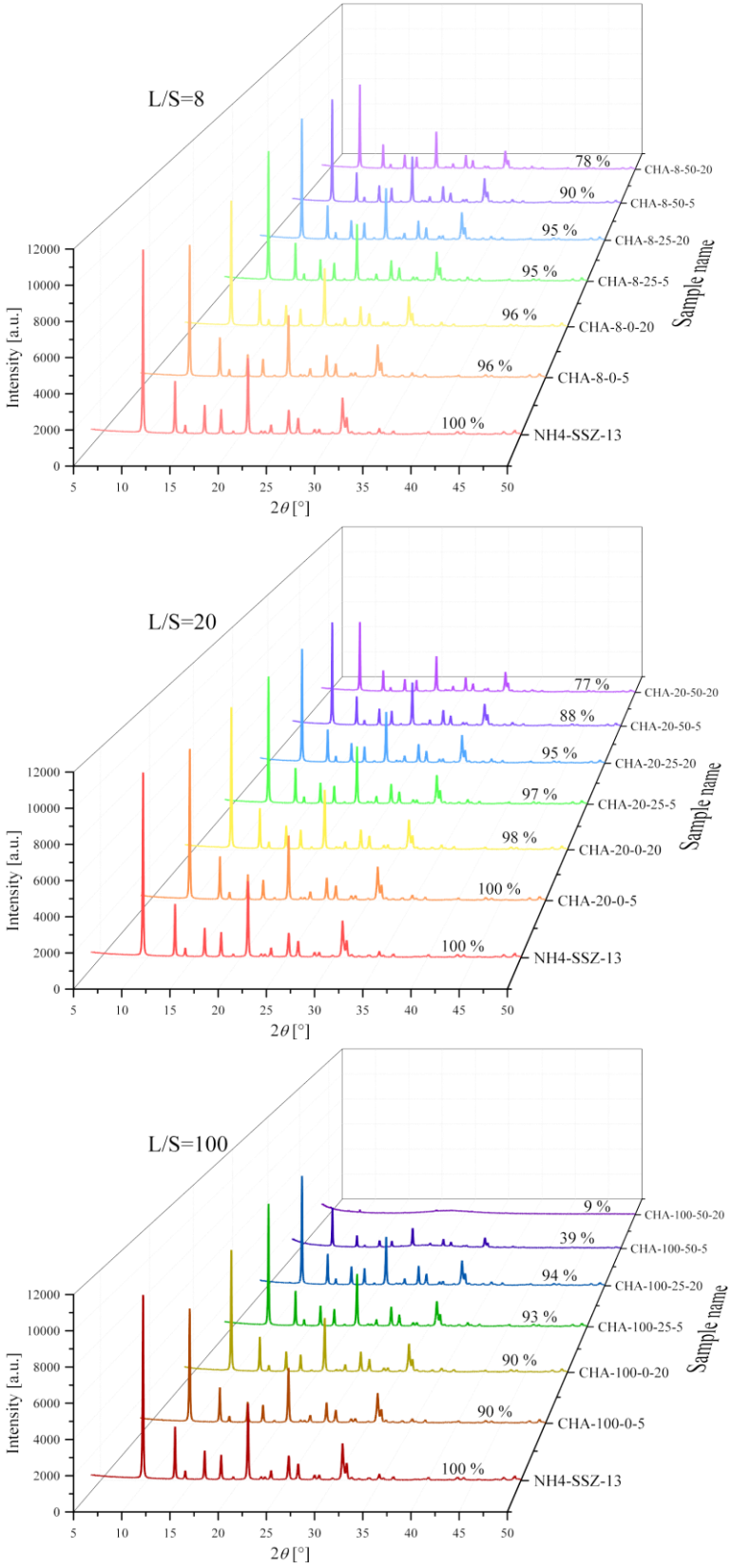

Figure 1. XRD patterns of etched derivatives and their parent NH_4-SSZ-13. Samples prepared with a liquid/solid ratio of 8, 20, and 100 are plotted. The relative (to the NH_4-SSZ-13 parent) crystallinity is indicated on each pattern.

SEM shows isometric SSZ-13 crystals with a cubic appearance. Their size ranges between 100 and 500 nm as the crystallites form larger agglomerates up to 1000 nm (**Figure S1**). The surface of parent crystals is flat with distinguishable edges and corners. The morphology of series I crystals is almost intact with minor signs of surface etching and separated intergrowths traces (**Figure 2A** and **B**). In series II (**Figure 2C** and **D**), more visible traces of etching are apparent. CHA-20-50-20 exhibits small holes (~10 - 40 nm) on the surface penetrating the crystals. The etching also removes parts of the crystals on the surface, eliminating intergrowths, and making the surface rougher. The effects of etching are more pronounced in series III (**Figure 2E** and **F**). CHA-100-0-20 displays holes in the mesopore range, penetrating in the crystals' core. A few cubic particles characteristic of SSZ-13 are visible in CHA-100-50-20. The sample also contains very small particles, most probably amorphous, with a random morphology.

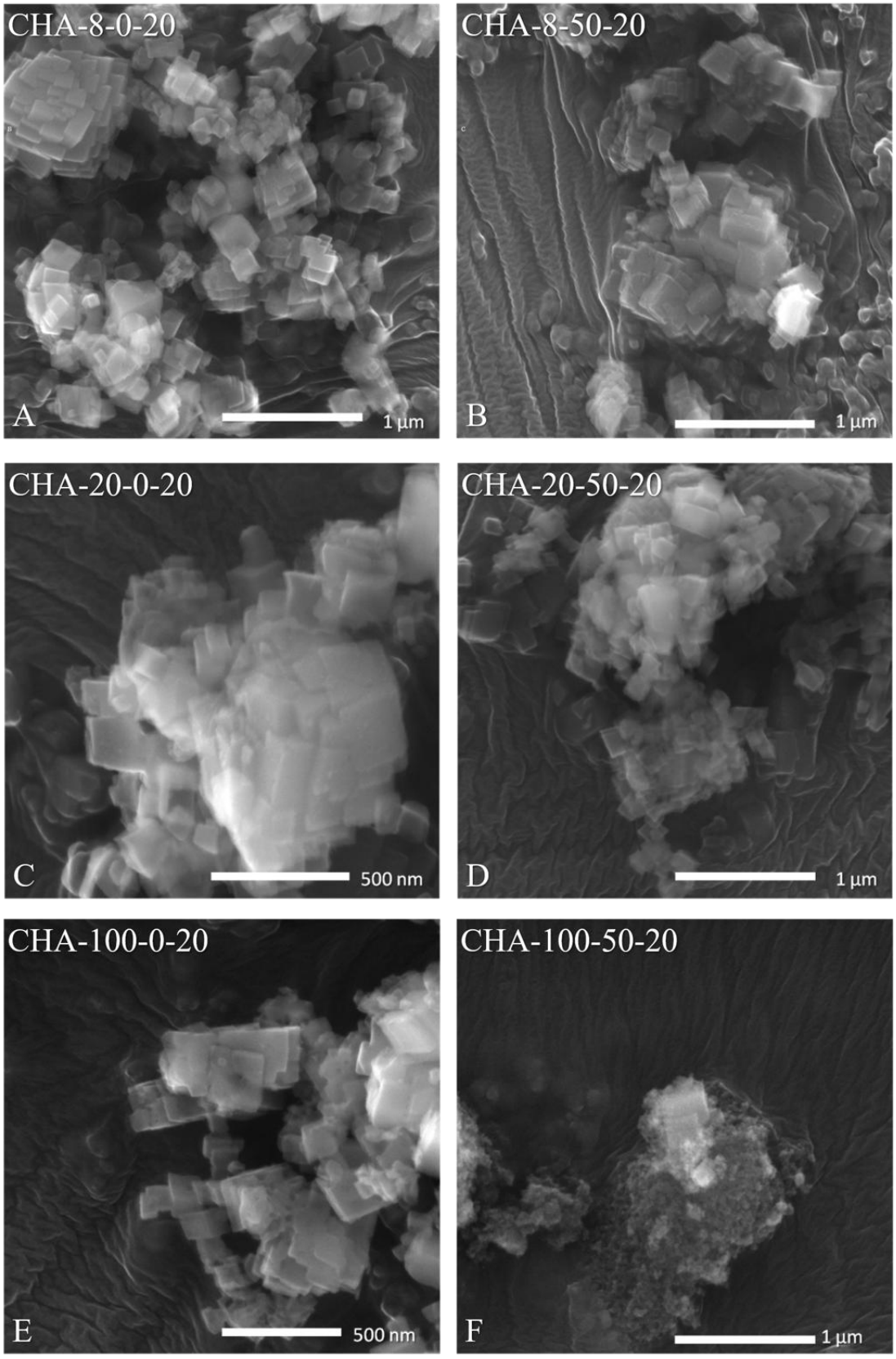

Figure 2. SEM micrographs of the etched samples: (A, B) series I, (C, D) series I, and (E, F) series III.

More details of series III samples etching were observed by TEM (**Figure 3**). CHA-100-25-5 (**Figure 3A**) exhibits a mostly regular cubic-like structure, with the average edges lengths of about 200 nm. The etching removes parts of crystals leaving porous crystals (a "swiss cheese"-like oval mesoporosity) with the outer edges of similar sizes as for the non porous crystals. CHA-100-25-20 (**Figure 3B**) is prepared as CHA-100-25-5 but with a 20 minutes etching. The surface of its crystals is rougher and marked by pores with depths up to 100 nm covering the entire crystal body on the facets surfaces. CHA-100-50-5 specimen (**Figure 3C)** exhibits two types of morphologies, very small particles most likely amorphous, with a foam type of structure, similar to those observed in CHA-100-50-20 by SEM (**Figure 2F**), and few cubic non-porous crystals.

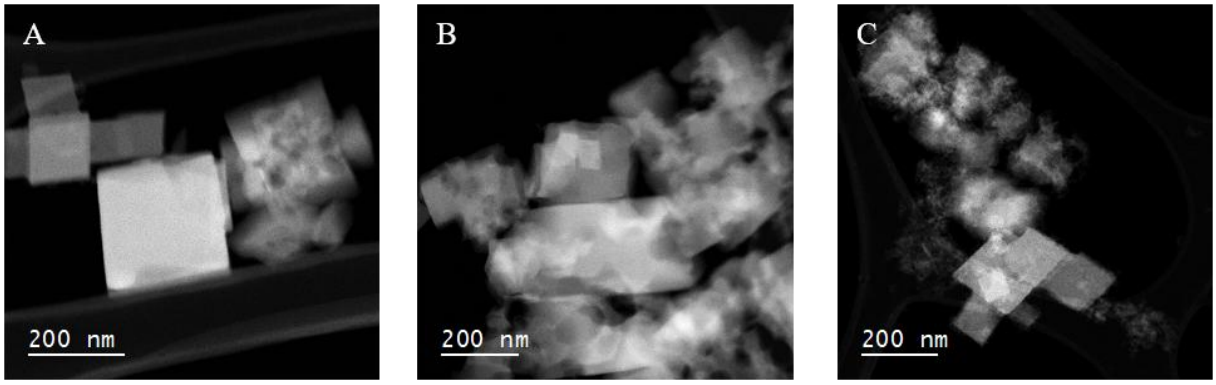

Figure 3. STEM-HAADF micrographs of: (A) CHA-100-25-5, (B) CHA-100-25-20 and (C) CHA-100-50-5.

N_2 physisorption curves are shown in **Figure 4.** The parent NH_4-SSZ-13 displays an I (a) type isotherm characteristic of microporous materials with a steep uptake at low relative pressure. The isotherm ends with an H4 hysteresis loop, characteristic of slit-type shape pores.[29] The analysis of the N_2 adsorption isotherms of the parent and its derivative is summarized in **Table 1**. The parent has a micropore volume of 0.27 $cm^3\ g^{-1}$, a mesopore volume of 0.04 $cm^3\ g^{-1}$, and a specific surface area of 700 $m^2\ g^{-1}$.

The etched samples display a high uptake in the micropore region, as they retain or even gain micropore volume compared to their parent. (**Figure 4**). In contrast, the severely etched samples, like CHA-100-50-5 and CHA-100-50-20, lose microporosity (**Figure 4E** and **F**). The textural changes are so profound in deeply etched samples that they exbibit a different isotherm. For instance, the CHA-100-50-20 isotherm has the features of type IV (a), and the hysteresis loop is an H1 type.[30]

The etched zeolites have mesopore volumes between 0.06 $cm^3\ g^{-1}$ and 0.98 $cm^3\ g^{-1}$, depending on the treatment conditions. In general, the etching close to 0 °C and at ambient temperature (25 °C) generate limited mesopore volume. Upon such conditions, the mesoporosity is not created at the expense of the native microporosity. A combination of high temperature and high l/s ratio etches the samples deeply and increases mesopore volume as in CHA-100-50-5 (0.75 $cm^3\ g^{-1}$) and CHA-100-50-20 (0.98 $cm^3\ g^{-1}$) but with loss of microporosity in both samples, CHA-100-50-5 having a decrease to 0.17 $cm^3\ g^{-1}$ and CHA-100-50-20 to 0.08 $cm^3\ g^{-1}$.

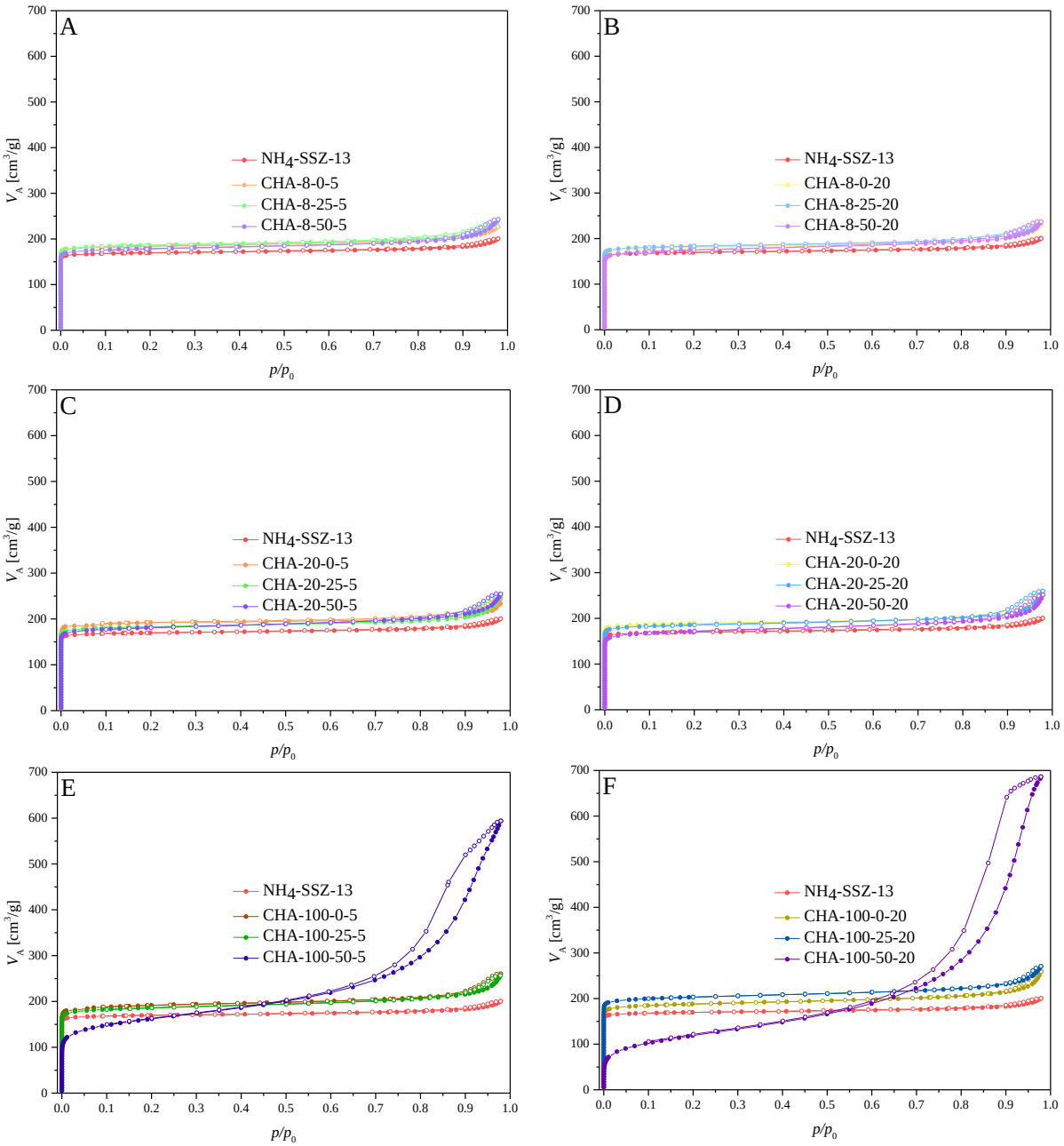

Figure 4. N_2 physisorption isotherms of series I (A, B), II (C, D), and III (E, F) samples.

Table 1. Physicochemical properties of parent and NH_4F etched samples.

	Sample	V_{micro} $cm^3\,g^{-1}$	V_{meso} $cm^3\,g^{-1}$	S_{BET} $m^2\,g^{-1}$	Si/Al_{ICP} mol mol^{-1}	Al_{ICP} µmol g^{-1}
	NH_4-SSZ-13	0.27	0.04	700	9.0	1234
Series I	CHA-8-0-5	0.29	0.06	758	9.1	1221
	CHA-8-25-5	0.29	0.08	765	9.0	1234
	CHA-8-50-5	0.28	0.10	728	10.2	1100
	CHA-8-0-20	0.28	0.07	745	9.0	1234
	CHA-8-25-20	0.29	0.08	752	9.7	1152
	CHA-8-50-20	0.27	0.10	700	10.6	1061
Series II	CHA-20-0-5	0.31	0.07	800	9.0	1234
	CHA-20-25-5	0.28	0.10	748	9.0	1234
	CHA-20-50-5	0.28	0.12	725	9.3	1197
	CHA-20-0-20	0.30	0.08	779	9.0	1234
	CHA-20-25-20	0.28	0.10	757	9.8	1141
	CHA-20-50-20	0.26	0.13	679	11.1	1017
Series III	CHA-100-0-5	0.30	0.11	780	9.5	1174
	CHA-100-25-5	0.29	0.11	750	9.9	1130
	CHA-100-50-5	0.17	0.75	522	29.5	400
	CHA-100-0-20	0.29	0.11	763	9.8	1141
	CHA-100-25-20	0.32	0.10	824	11.4	992
	CHA-100-50-20	0.08	0.98	309	287.9	42

The parent NH_4-SSZ-13 has a Si/Al_{ICP} ratio of 9 (**Table 1**). In series I and II, the Si/Al ratio is mostly maintained and fluctuates between 9 – 11 even at the highest temperature (50 °C). More significant changes in the Si/Al ratio occur in series III at 50 °C treatment when Si/Al reaches 30 and 288 (**Table 1**). These materials, however, are partially or fully amorphized (**Figure 1**).

The Si/Al ratios obtained by STEM-EDS analysis are shown in **Figure S2.** The Si/Al ratio observed for samples CHA-100-25-5, CHA-100-25-20, and CHA-100-50-5 differ from the ICP-AES method results. In samples CHA-100-25-5 and CHA-100-25-20, the silicon content is 3 to 4 fold higher. CHA-100-50-5 sample has zones that are significantly depleted of Al, and the observed ratio is 1.4 to 19 folds higher than the ratio found by ICP-AES. The fluctuation of Si and Al content in different crystals is attributed to the different levels of amorphization. These results illustrate that the crystallinity lost is related to a preferential

dealumination. Also, there is a gradient of Al concentration in deeply etched samples, as the surface and the core of a crystal can exhibit different framework composition.

While ICP provides a bulk composition, ^{27}Al MAS NMR will distinguish between framework and extra-framework aluminum. **Figure 5** summarizes aluminum's state in the parent and the derivatives from series I, II, and III. All spectra display three peaks, often encountered in zeolites. The peak at 58 ppm is characteristic of the framework, tetrahedrally coordinated aluminum. The broad tailing between 50 and 30 ppm is attributed to distorted tetrahedral or penta-coordinated aluminum. The low-intensity broad peak between 0 and -10 ppm is due to extraframework hexacoordinated aluminum species.

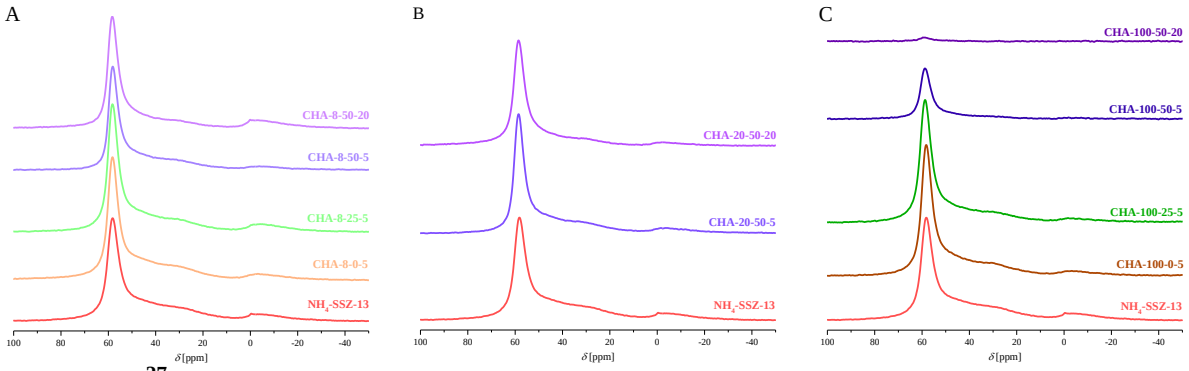

Figure 5. ^{27}Al MAS NMR spectra of the non-calcined samples from (A) series I, (B) series II, and (C) series III.

The peak intensities of zeolites in series I (**Figure 5A**) and II (**Figure 5B**) are mostly preserved. In contrast, the deeply etched samples from series III (CHA-100-50-5 and CHA-100-50-20) show a substantial decrease in peak intensities (**Figure 5C)**. **Table 2** summarizes the ICP and ^{27}Al MAS NMR results. The data show an increase in extra framework Al after calcination, which is below 20 % of overall Al content for most tested samples, except CHA-8-0-5 and CHA-8-25-5. The amount of Al, which remains in tetrahedral coordination and provides a Brønsted acid site, is evaluated. As can be seen, the sample treated under mild conditions retains the number of Brønsted acid sites.

Table 2. Chemical composition of the samples obtained from ICP-AES and ^{27}Al MAS NMR data.

	As-synthesized				Calcined
Sample	Si/Al_{ICP}	Al_{ICP}	$Al^{IV}{}_{NMR}$	Si/Al^{IV}	Al^{VI}
	mol mol^{-1}	µmol g^{-1}	µmol g^{-1}	mol mol^{-1}	%
NH_4-SSZ-13	9.0	1234	1101	10.1	27.2
CHA-8-0-5	9.1	1221	1131	9.8	24.2
CHA-8-25-5	9.0	1234	1113	10.0	30.3
CHA-8-50-5	10.2	1100	1028	10.9	18.5
CHA-8-50-20	10.6	1061	923	12.2	/
CHA-20-50-5	9.3	1197	1105	10.1	/
CHA-20-0-20	9.0	1234	/	/	19.4
CHA-20-25-20	9.8	1141	/	/	17.9
CHA-20-50-20	11.1	1017	966	11.7	18.6
CHA-100-0-5	9.5	1174	1102	10.1	/
CHA-100-25-5	9.9	1130	1066	10.5	/
CHA-100-50-5	29.5	400	373	31.7	/
CHA-100-0-20	9.8	1141	/	/	17.4
CHA-100-50-20	287.9	42	42	287.9	/

^{29}Si MAS NMR is also a reliable technique to measure the Si/Al framework composition. **Figure 6** highlights the spectra of the NH_4-SSZ-13 parent and one derivative (CHA-20-50-20). Both spectra exhibit three peaks at chemical shifts (δ) -111, -105, and -99 corresponding to Si(4Si, 0Al), Si(3Si, 1Al) and Si(2Si, 2Al), respectively.[31] The magnitude of resonance peaks is strongly impacted by the number of the neighboring framework atoms, and Al as the nearest neighbor has a strong influence on the intensity of those peaks.[32] Sample CHA-20-50-20 shows the decreased intensity of the resonance peaks corresponding to Si(4Si, 0Al), Si(3Si, 1Al). The decreasing intensity of the resonance peaks is related to a decreasing number of neighboring Al atoms.

^{29}Si{^{1}H} cross-polarization NMR gives qualitative information on the silanol species in zeolites. The spectra of the parent and CHA-20-50-20 simple are depicted in **Figure S3**. The parent material exhibits resonance peaks in the area -110 to -90 ppm. In this range, there is some overlap of the peaks related to Si-O-Al and Si-O-OH. Sample CHA-20-50-20 shows an increase of the peak intensity in the -110 to -90 ppm region, which is attributed to a rise in Si-OH group concentration. The extraction of a framework atom results in the formation of silanol groups highlighted by the ^{29}Si{^{1}H} cross-polarization NMR spectrum changes.

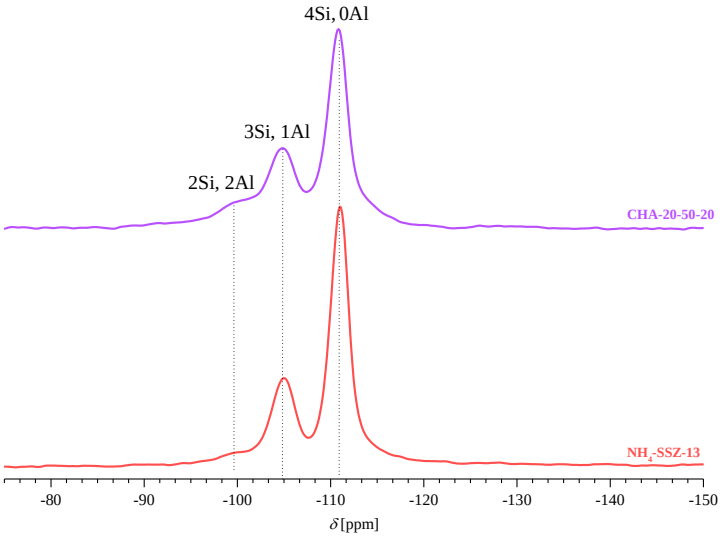

Figure 6. ^{29}Si MAS NMR spectra of NH_4-SSZ-13 and one derivative, CHA-20-50-20.

^{19}F MAS NMR (**Figure S4**) is a very sensitive technique able to detect traces (ppb) of fluor in solids.[33] We employed this technique to verify if the etched zeolites retain some fluorinated products. All spectra ^{19}F MAS NMR shows a broad peak around -103 ppm due to the PTFE signal from the rotor cap. Besides, several weak peaks were observed in CHA-100-50-20, CHA-20-50-20, and CHA-8-50-20 samples. These peaks emanate from the etching reaction products, as -169, -152, -140, and -125 ppm resonances reveal the presence of SiF_4, Na_2SiF_6, $(NH_4)_3AlF_6$, and $(NH_4)_2SiF_6$, respectively. The peaks' intensity is low, showing the low content of these products. After calcination, the traces of fluorine compounds disappeared.

The acidity of the etched zeolites is studied by IR spectroscopy using deuterated acetonitrile as a probe molecule. CD_3CN adsorbed on acid sites is detected in the 2400-2200 cm^{-1} spectral window (**Figure S5**). The deconvolution of the 2360 – 2180 cm^{-1} spectral range reveals five peaks (**Figure S6**), four sharp at 2324, 2316, 2295, 2283, 2265 cm^{-1}, and a broad one centered at 2214 cm^{-1}. The 2283 cm^{-1} peak is attributed to CD_3CN interacting with silanols as observed on a purely siliceous material MFI-type material.[34] The 2324 cm^{-1} peak corresponds to CD_3CN interacting with Lewis acid sites [35] while the 2265 cm^{-1} corresponds to physisorbed CD_3CN. The 2298 cm^{-1} peak results from CD_3CN interacting with Brønsted acid sites while the attribution of the 2310 cm^{-1} peak is a matter of debate and could be due to CD_3CN interacting with either weak Lewis acid sites [28] or weak Brønsted acid sites.[36] The acid site concentrations, Brønsted (c_B), and Lewis (c_L), are summarized in **Table 3**. The Brønsted

acidity is preserved on all etched samples except for some deeply etched ones from series III (CHA-100-25-20, CHA-100-50-5) where their Lewis acidity increases.

Here, we define the accessibility index (ACI) as the number of acid sites ($c_{B+}c_L$) detected by CD_3CN adsorption divided by the total amount of acid sites in the zeolite, based on the measured aluminum content (Al_{ICP}).[37] In the parent NH_4-SSZ-13, ACI is 0.47. The etched zeolites in series I and II have ACI in the range 0.52 - 0.61, while under more severe conditions as in series III, ACI increases to 0.70 for CHA-100-50-5. The latter zeolite, however, lost much of its Brønsted acidity.

Table 3. Acid site concentrations of the parent H-SSZ-13 and its etched derivatives.

Sample	**Al_{ICP}**	**c_L**	**c_B**	**$c_B + c_L$**	**ACI**
	µmol g^{-1}	µmol g^{-1}	µmol g^{-1}	µmol g^{-1}	/
H-SSZ-13	1234	176	401	577	0.47
CHA-20-0-5	1234	245	400	645	0.52
CHA-20-0-20	1234	276	396	672	0.54
CHA-20-25-5	1234	322	413	735	0.60
CHA-20-50-5	1197	205	417	622	0.52
CHA-20-25-20	1141	240	371	611	0.54
CHA-20-50-20	1017	288	330	618	0.61
CHA-100-25-20	992	251	285	536	0.54
CHA-100-50-5	400	59	222	281	0.70

The activated parent sample was studied by IR spectroscopy. The OH region's deconvolution reveals the presence of a series of bands in the 3750 – 3450 cm^{-1} range (**Figure S7)**. The etched samples showed similar spectra with the exceptions of samples CHA-20-50-20 and CHA-100-50-5, where silanol bands become more prominent (**Figure 7**). As the CHA structure contains one T-site and four crystallographically different oxygen atoms, four possible acid site configurations are possible.[38] Suzuki et al. attribute the ~3644, ~3616, ~3575, and ~3538 cm^{-1} bands to acidic OH groups on four nonequivalent oxygen sites in the CHA structure.[39] The complex peak at 3742 cm^{-1} with a shoulder at 3735 cm^{-1} band

represents isolated silanols, on the external surface of the zeolite and in internal position in the zeolite, respectively, while the 3716 cm^{-1} band is related to vicinal silanol groups.[38] The bridged hydroxyls (Brønsted acid sites) are observed as a composite band centered around 3612 cm^{-1} with a shoulder at 3594 cm^{-1}. The bands 3660 – 3680 cm^{-1} indicate the presence of an extra framework or distorted framework aluminum.[38]

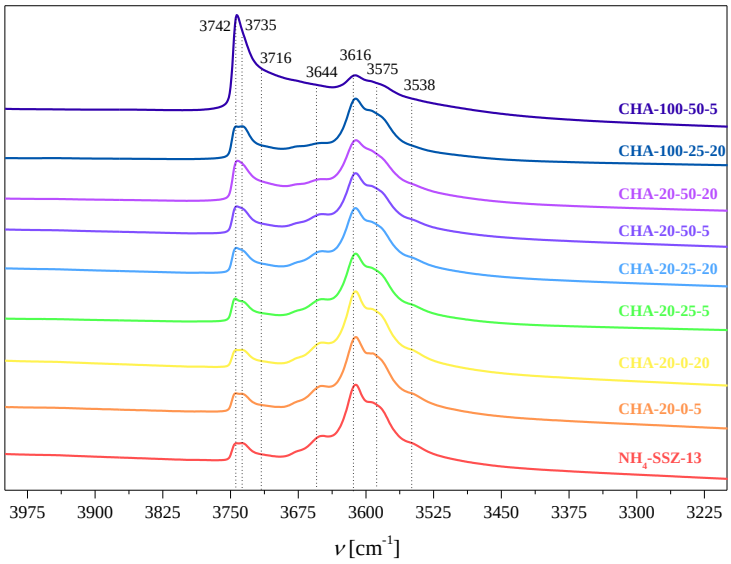

Figure 7. Room temperature IR spectra of the pristine surface hydroxyls of the H-SSZ-13 zeolite and its derivatives after activation (T: 450 °C).

The dehydration of n-propanol is a reaction catalyzed by Brønsted acid sites. We have employed this reaction to screen the catalytic properties of the hierarchical derivatives of SSZ-13. Under our conditions (T= 205 °C, P= 1 bar, W/F°= of 27.2 kg mol^{-1} s), the protonic form of the parent has an initial conversion of 94 %, but it decreases fast with time on stream (TOS) (**Figure 8**). After 10 minutes of TOS, the conversion falls to about 30 %. All etched samples have a similar initial conversion, between 85 and 95 %, with sample CHA-8-50-5 having the highest (97 %) initial conversion.

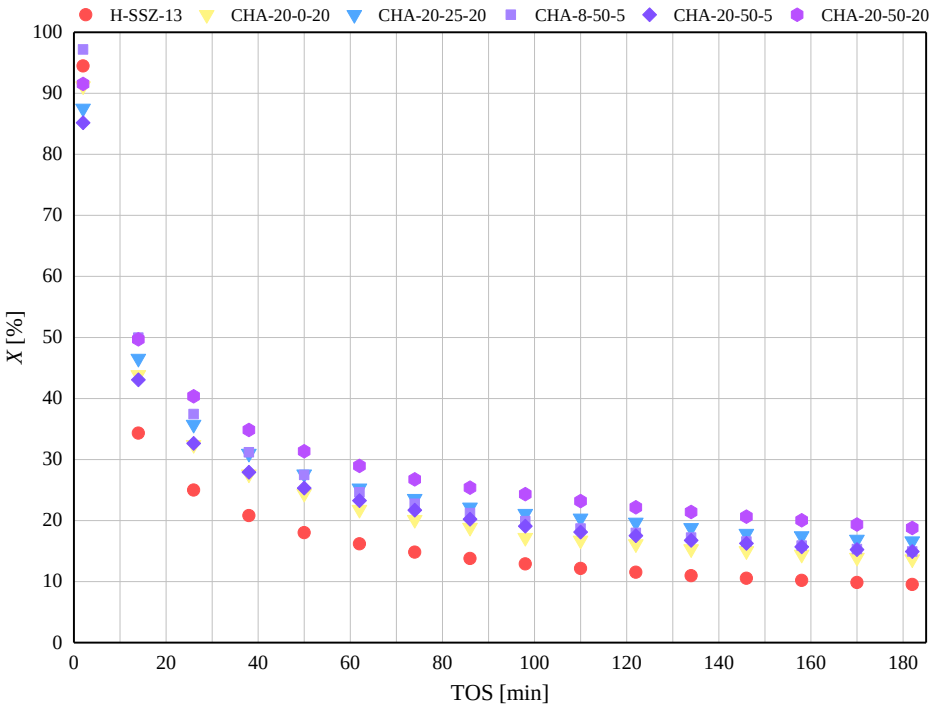

Figure 8. The n-propanol conversion (*X* [%]) with time on stream (TOS [min]) for the H-SSZ-13 parent and some NH_4F etched derivatives (T=205 °C, P=1 bar, W/F°= 27.2 kg mol^{-1} s).

The parent sample exhibits significant propene selectivity, yielding also small amounts of dipropyl ether and propanal. Heavier products (C_{4+}) were observed in the outlet gas in very small quantities <0.03 %, which is consistent with a previous study, where heavier products are yielded at higher reaction temperatures.[40] In our experiments, these products appeared in detectable amounts at temperatures above 230 °C. The parent sample's selectivity toward propene decreases with the decrease of the conversion (**Figure 9**). In general, the etched samples show higher selectivity to propene than the parent, as selectivity decreases in the order CHA-20-50-20> CHA-20-50-5> CHA-8-50-5> CHA-20-25-20> CHA-20-0-20> H-SSZ-13.

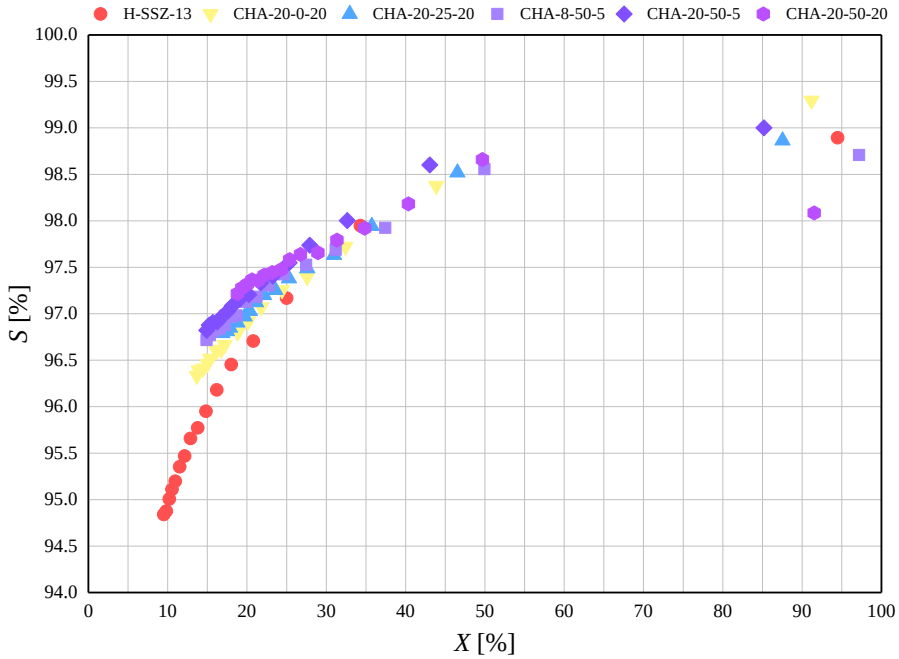

Figure 9. Propene selectivity (y-axis) as a function of propanol conversion (x-axis) for parent and etched samples.

Coke content in the exhausted catalysts was estimated by thermogravimetric analysis (**Table S1**), as the mass loss between 200 and 800 °C was attributed to coke removal. Total coke loss of the parent sample is 11.4 %. The coke content in the etched samples was slightly higher, ranging between 12 and 14.5 %.

4 Discussion

Relatively concentrated (40 *w*/%) NH_4F aqueous solution was used to obtain hierarchical SSZ-13 zeolites. The etching conditions, including the liquid/solid ratio, treatment temperature, and time, were varied to obtain materials with different physicochemical properties. Hydrothermal treatment with an aqueous ammonium fluoride solution is a proven zeolite etching method.

The NH_4F etching of SSZ-13 generates mesopores in all prepared samples, including the most mildly treated one. For example, CHA-8-0-5 from series I show a slight increase of the mesopore volume (V_{meso}= 0.06 $cm^3\ g^{-1}$) in comparison to the parent zeolite (V_{meso}= 0.04 $cm^3\ g^{-1}$). The tuning of etching parameters allowed to increase mesoporosity and retain the basic characteristics of parent zeolite in terms of crystallinity, micropore volume, and acidity. For instance, sample CHA-20-50-20, which is representative of this series of samples, its mesopore volume increases to 0.13 $cm^3\ g^{-1}$. Much higher mesopore volume is observed in the sample subjected to partial amorphization. For instance, the CHA-100-50-20 sample reached a mesopore volume of 0.98 $cm^3 g^{-1}$, but the micropore volume dropped to 0.08 $cm^3\ g^{-1}$.

The most significant changes in the physicochemical properties were observed for the zeolites etched at 50 °C. Their relative crystallinity is usually below 90 % and can drop to 9 % when a liquid/solid ratio of 100 is used. N_2 physisorption data matches well with XRD analysis and changes in the chemical composition analyzed by ICP-AES. The samples of series III (l/s= 100) have a loss of micropore volume after 5 minutes of etching (0.17 $cm^3\ g^{-1}$), and after 20 minutes of etching, the micropore volume drops to 0.08 $cm^3\ g^{-1}$ when compared w ith the parent zeolite (0.27 $cm^3\ g^{-1}$). In contrast, the samples prepared at lower temperatures (0 and 25 °C) have a well-preserved micropore volume or even higher than the parent zeolite. For instance, several samples exhibit a micropore volume from 0.28 to 0.32 $cm^3\ g^{-1}$. We attribute the last phenomenon to the dissolution of low crystalline or amorphous material present in the sample. The etching at 50 °C causes loss of crystallinity revealed by the lower intensity of the XRD peaks and a loss of micropore volume. The etching at this temperature generates amorphous material that could remain, thus causing a pore blockage.

Micrographs obtained by SEM reveal changes in the surface morphology of the etched samples (**Figure 2**). In the case of SSZ-13, the small intrinsic pores (0.38 nm) impose diffusion limitations to the water-fluoride species. Consequently, the etching reaction is

concentrated at the crystal surface, and the dissolution rate rises at an elevated temperature (50 °C). Thus, the treatment at 50 °C (CHA-100-50-20) resulted in foam-like particles after only 20 min of treatment (**Figure 3C**). Micrographs from series I samples show the etching is generally started from the surface and removes parts of the crystal vulnerable to NH_4F dissolution, defect zones, and nanocrystalline domains. A similar type of dissolution in a fluoride medium has already been reported.[41,42] The number of "holes" created by NH_4F is multiplied for the series II and III samples, showing more intense zeolite dissolution at a higher l/s ratio. Finally, increasing the etching time also leads to the deeper dissolution of zeolite crystals (**Figure 3A** and **B).**

The results of chemical composition analysis (**Table 1**) show a non-selective extraction of framework cations. Even the most deeply treated series I and II samples have a Si/Al ratio of 11, which is not substantially different from the parent material. The changes in the framework composition of series III samples are still in this range when the treatment is performed at 0 and 25 °C. Only samples CHA-100-50-5 and CHA-100-50-20 treated at 50 °C show substantial dealumination, which is related to an almost total loss of crystallinity. The EDX results imply the Al is not evenly distributed within the etched crystals. In addition the surface of the crystals is more attacked since it contains less aluminum, particularly in the case of partially amorphous samples. Such a type of dissolution is most probably due to the diffusion limitation of water-soluble fluoride anions through the pores of SSZ-13. This was also observed in the work of Bolshakov et al. while treating ZSM-5 with NH_4F solution.[43]

Solid-state ^{27}Al MAS NMR was used to evaluate the state of Al in the etched samples (**Figure 5C, Table 2**). Overall, the samples from series I and II show preserving the chemical shift intensities with respect to the parent, *i.e.*, no substantial changes in the state of Al take place during the fluoride etching. Furthermore, the data collected show that the NH_4F etching does not contribute to the octahedral extra framework aluminum formation. The acidity measurements show that the Brønsted acid site's concentration is preserved for the series I and II samples, further confirming the NMR data. The samples from series III have lower Brønsted acid site concentrations (**Table 3**). The concentration of Lewis acid sites is increased for all three series of samples, which is attributed to products of the etching reaction.

The catalytic activity of parent and modified zeolites was tested in the dehydration of n-propanol. Primary alcohols undergo dehydration via the E_2 elimination mechanism, where dipropyl ether are intermediates of acid-catalyzed dehydration of alcohols.[44] Here, dipropyl

ether is observed as a minor product of the reaction along with propanal, while the propene is yielded with high selectivity (>90 %). Ethers normally form as major products at temperatures lower than 200 °C. Propanal formation indicates some oxidation reaction occurs along with dehydration and dehydrogenation reactions. The parent and treated samples' initial activity was similar, i.e., in the range of 85 - 95 %, reflecting a similar number of available active sites. Differences were observed with the extension of the time on stream, where the etched samples, as a function of the treatment conditions, showed lower deactivation. Oligomers (C_{4+}) and coke formation are most likely the cause. Oligomers are formed at the beginning of the reaction in small amounts (~0.9 %). After the first 2 min, their conversion is reduced (0.03 %). The etched samples also have a higher selectivity towards propene; this is most likely due to generated hierarchical porosity and the small changes in the Si/Al ratio. As known, the dehydrogenation reaction of n-propanol yielding dipropyl ether takes place mainly on the flat surface of the catalyst, whereas the dehydration reaction is restricted to the pores.[45] Therefore, the increased porosity in hierarchical zeolites promotes the later reaction. Zhi et al. described these mechanisms of dimer formation and alkoxide formation during n-propanol dehydration over ZSM-5.[46] A dehydration reaction is also inhibited by the presence of water, which is the co-product competing with alcohol reactants for BAS.[46,47]

The etched catalysts showed extended lifetime and higher coke content to the parent. The improved activity of etched derivatives is certainly related to the enhanced accessibility to active sites, together with the preserved Brønsted acidity. Previous spectroscopic data suggest the large carbonaceous species from the near-surface region of the crystals.[48,49] Thus, the deactivation is slower, with the sample having a higher external surface due to introduced mesopores

Previous studies of NH_4F or HF buffered with NH_4F etching focused on medium-pore (10MR) zeolites like MFI and FER and large-pore (12MR) zeolites like FAU, LTL, MOR, and Beta.[42,50–53] Compared with previous studies, the dissolution of the small-pore SSZ-13 shows some differences. For instance, Qin et al. also used 40 *w*/% NH_4F solutions to etch ZSM-5 upon similar experimental conditions. They reported rapid and abundant mesopore formation in the case of ZSM-5.[42] We attribute the slower dissolution rate of SSZ-13 to the small pore size. The diffusion of hydrated bi-fluoride ion through the 8MR window of the chabazite cage is restrained. Thus, only the surface defects are the available sites where the dissolution can start. Consequently, the surface etching dominates the dissolution process when mild etching conditions are employed. The last statement is supported by the preserved

micropore volume in most of the treated samples. The substantial micropore volume loss is only noticeable in extreme cases, *i.e.*, when the etching temperature is 50 °C, accelerating the etching reaction, and the liquid/solid ratio is high. Briefly, the dissolution rate of SSZ-13 is particularly lower compared with the larger pore zeolites.

5 Conclusion

Hierarchical zeolite SSZ-13 was successfully obtained by post-synthesis etching with a 40 *w*/% NH_4F water solution. The effect of each parameter influencing the zeolite dissolution, *i.e.*, the temperature, liquid/solid ratio, and time, was studied, and the conditions of etching optimized. Using ambient temperature and low liquid/solid ratio (8 and 20) leads to hierarchical SSZ-13 derivatives with retained intrinsic characteristics. More precisely, the crystallinity, micropore volume, and the number of Brønsted acid sites were similar to the parent zeolite. Consequently, these hierarchical materials showed improved catalytic stability in the dehydration of n-propanol. Solely an extended treatment at 50 °C resulted in a partial amorphization of the zeolite and alteration of its physicochemical properties.

The results of this study revealed some particularities of the dissolution of small-pore zeolites in a fluoride medium. The dissolution rate is lower, although relatively concentrated NH_4F solution was used, which is attributed to the constrained diffusion of hydrated bi-fluoride ions through the small pore channels. Consequently, the mesopore generation always starts from the crystal surface and penetrates further into the crystal's bulk. This particularity of SSZ-13 NH_4F etching is probably valid for all small pore zeolites.

Acknowledgments

V.B. acknowledges the PhD grant (RIN 100) from the Normandy region. J.-P.G., N.N., and V.V. acknowledge the Industrial Chair ANR-TOTAL “NanoCleanEnergy” (ANR-17-CHIN-0005-01) and FEDER 18P01675 contract for financial support. SK, SM and VV acknowledge the financial support of Carnot Institute (Energie et Systeme de Propulsion), the 3DNanoZET project. GENESIS is supported by the Région Haute-Normandie, the Métropole Rouen Normandie, the CNRS via LABEX EMC and the French National Research Agency as a part of the program “Investissements d’avenir” with the reference ANR-11-EQPX-0020.

References

[1] C. Colella, Stud. Surf. Sci. Catal. 157 (2005) 13–40. https://doi.org/10.1016/S0167-2991(05)80004-7

[2] A.F. Masters, T. Maschmeyer, Microporous Mesoporous Mater. 142 (2011) 423–438. https://doi.org/10.1016/j.micromeso.2010.12.026.

[3] J. Kärger, D. M. Ruthven, D. N. Theodorou, Diffusion in Nanoporous Materials, Wiley-Blackwell, 2012, pp. 561–606.

[4] L.S. Dent, J.V. Smith, Nature. 181 (1958) 1794–1796. https://doi.org/10.1038/1811794b0

[5] V. Van Speybroeck, K. Hemelsoet, K. De Wispelaere, Q. Qian, J. Van der Mynsbrugge, B. De Sterck, B.M. Weckhuysen, M. Waroquier, ChemCatChem. 5 (2013) 173–184. https://doi.org/10.1002/cctc.201200580

[6] Z. Li, M.T. Navarro, J. Martínez-Triguero, J. Yu, A. Corma, Catal. Sci. Technol. 6 (2016) 5856–5863. https://doi.org/10.1039/C6CY00433D

[7] P. Tian, Y. Wei, M. Ye, Z. Liu, ACS Catal. 5 (2015) 1922–1938. https://doi.org/10.1021/acscatal.5b00007

[8] F. Bleken, M. Bjørgen, L. Palumbo, S. Bordiga, S. Svelle, K.-P. Lillerud, U. Olsbye, Top. Catal. 52 (2009) 218–228. https://doi.org/10.1007/s11244-008-9158-0

[9] E. Koohsaryan, M. Anbia, Chin. J. Catal. 37 (2016) 447–467. https://doi.org/10.1016/S1872-2067(15)61038-5

[10] A.M. Beale, F. Gao, I. Lezcano-Gonzalez, C.H.F. Peden, J. Szanyi, Chem. Soc. Rev. 44 (2015) 7371–7405. https://doi.org/10.1039/C5CS00108K.

[11] V. Valtchev, G. Majano, S. Mintova, J. Pérez-Ramírez, Chem. Soc. Rev. 42 (2012) 263–290. https://doi.org/10.1039/C2CS35196J

[12] R. Oord, I.C. ten Have, J.M. Arends, F.C. Hendriks, J. Schmidt, I. Lezcano-Gonzalez, B.M. Weckhuysen, Catal. Sci. Technol. 7 (2017) 3851–3862. https://doi.org/10.1039/C7CY00798A.

[13] L. Sommer, D. Mores, S. Svelle, M. Stöcker, B.M. Weckhuysen, U. Olsbye, Microporous Mesoporous Mater. 132 (2010) 384–394. https://doi.org/10.1016/j.micromeso.2010.03.017

[14] M.K. Wardani, G.T.M. Kadja, A.T.N. Fajar, Subagjo, I.G.B.N. Makertihartha, M.L. Gunawan, V. Suendo, R.R. Mukti, RSC Adv. 9 (2019) 77–86. https://doi.org/10.1039/C8RA08979E

[15] H.S. Shin, I.J. Jang, N.R. Shin, S.H. Kim, S.J. Cho, Res. Chem. Intermed. 37 (2011) 1239–1246. https://doi.org/10.1007/s11164-011-0390-z

[16] W. Dai, X. Sun, B. Tang, G. Wu, L. Li, N. Guan, M. Hunger, J. Catal. 314 (2014) 10–20. https://doi.org/10.1016/j.jcat.2014.03.006

[17] L. Sommer, A. Krivokapić, S. Svelle, K.P. Lillerud, M. Stöcker, U. Olsbye, J. Phys. Chem. C. 115 (2011) 6521–6530. https://doi.org/10.1021/jp109696z

[18] S.I. Zones, L.-T. Yuen, S.J. Miller, Small crystallite zeolite CHA, US6709644B2, 2004.

[19] L. Wu, V. Degirmenci, P.C.M.M. Magusin, B.M. Szyja, E.J.M. Hensen, Chem. Commun. 48 (2012) 9492–9494. https://doi.org/10.1039/C2CC33994C

[20] L. Wu, V. Degirmenci, P.C.M.M. Magusin, N.J.H.G.M. Lousberg, E.J.M. Hensen, J. Catal. 298 (2013) 27–40. https://doi.org/10.1016/j.jcat.2012.10.029

[21] X. Zhu, J.P. Hofmann, B. Mezari, N. Kosinov, L. Wu, B.M. Weckhuysen, S. Asahina, J. Ruiz-Martínez, ACS Catal. 6 (2016) 2163–2177. https://doi-org.inc.bib.cnrs.fr/10.1021/acscatal.5b02480

[22] X. Zhu, R. Rohling, G. Filonenko, B. Mezari, J.P. Hofmann, S. Asahina, E.J.M. Hensen, Chem. Commun. 50 (2014) 14658–14661. https://doi.org/10.1039/C4CC06267A

[23] B. Liu, X. Zhao, W. Mao, H. Chen, L. Han, K. Zhu, X. Zhou, Microporous Mesoporous Mater. 285 (2019) 202–214. https://doi.org/10.1016/j.micromeso.2019.05.004
[24] K.-G. Haw, S. Moldovan, L. Tang, Z. Qin, Q. Fang, S. Qiu, V. Valtchev, Inorg. Chem. Front. 7 (2020) 2154–2159. https://doi.org/10.1039/D0QI00261E
[25] V. Valtchev, J.-P. Gilson, Z. Qin, Method for the preparation of synthetic crystalline zeolite materials with enhanced total pore volume, WO2016005783 A1.
[26] Z. Qin, L. Lakiss, J.-P. Gilson, K. Thomas, J.-M. Goupil, C. Fernandez, V. Valtchev, Chem. Mater. 25 (2013) 2759–2766. https://doi.org/10.1021/cm400719z
[27] T. Usui, Z. Liu, H. Igarashi, Y. Sasaki, Y. Shiramata, H. Yamada, K. Ohara, T. Kusamoto, T. Wakihara, ACS Omega. 4 (2019) 3653–3659. https://doi.org/10.1021/acsomega.8b03409
[28] B. Wichterlová, Z. Tvarůžková, Z. Sobalík, P. Sarv, Microporous Mesoporous Mater. 24 (1998) 223–233. https://doi.org/10.1016/S1387-1811(98)00167-X
[29] M. Thommes, K. Kaneko, A.V. Neimark, J.P. Olivier, F. Rodriguez-Reinoso, J. Rouquerol, K.S.W. Sing, Pure Appl. Chem. 87 (2015) 1051–1069. https://doi.org/10.1515/pac-2014-1117
[30] K.A. Cychosz, R. Guillet-Nicolas, J. García-Martínez, M. Thommes, Chem. Soc. Rev. 46 (2017) 389–414. https://doi.org/10.1039/C6CS00391E
[31] G. Engelhardt, TrAC, Trends Anal. Chem. 8 (1989) 343–347. https://doi.org/10.1016/0165-9936(89)87043-8.
[32] J.M. Newsam, J. Phys. Chem. 89 (1985) 2002–2005. https://doi.org/10.1021/j100256a040
[33] J.M. Griffin, J.R. Yates, A.J. Berry, S. Wimperis, S.E. Ashbrook, J. Am. Chem. Soc. 132 (2010) 15651–15660. https://doi.org/10.1021/ja105347q.
[34] C. Pazé, S. Bordiga, G. Spoto, C. Lamberti, A. Zecchina, J. Chem. Soc., Faraday Trans. 94 (1998) 309–314. https://doi.org/10.1039/A705380K
[35] R.E. Sempels, P.G. Rouxhet, J. Colloid Interface Sci. 55 (1976) 263–273. https://doi.org/10.1016/0021-9797(76)90033-3
[36] W. Daniell, N.-Y. Topsøe, H. Knözinger, Langmuir. 17 (2001) 6233–6239. https://doi.org/10.1021/la010345a
[37] F. Thibault-Starzyk, I. Stan, S. Abelló, A. Bonilla, K. Thomas, C. Fernandez, J.-P. Gilson, J. Pérez-Ramírez, J. Catal. 264 (2009) 11–14. https://doi.org/10.1016/j.jcat.2009.03.006
[38] S. Bordiga, L. Regli, D. Cocina, C. Lamberti, M. Bjørgen, K.P. Lillerud, J. Phys. Chem. B. 109 (2005) 2779–2784. https://doi.org/10.1021/jp045498w
[39] K. Suzuki, G. Sastre, N. Katada, M. Niwa, Phys. Chem. Chem. Phys. 9 (2007) 5980–5987. https://doi.org/10.1039/B711961E
[40] A.W. Lepore, Z. Li, B.H. Davison, G.-S. Foo, Z. Wu, C.K. Narula, Ind. Eng. Chem. Res. 56 (2017) 4302–4308. https://doi.org/10.1021/acs.iecr.7b00592
[41] Z. Qin, J.-P. Gilson, V. Valtchev, Curr. Opin. Chem. Eng. 8 (2015) 1–6. https://doi.org/10.1016/j.coche.2015.01.002
[42] Z. Qin, G. Melinte, J.-P. Gilson, M. Jaber, K. Bozhilov, P. Boullay, S. Mintova, O. Ersen, V. Valtchev, Angew. Chem. 128 (2016) 15273–15276. https://doi.org/10.1002/ange.201608417
[43] A. Bolshakov, N. Kosinov, D.E.R. Hidalgo, B. Mezari, A.J.F. van Hoof, E.J.M. Hensen, Catal. Sci. Technol. 9 (2019) 4239–4247. https://doi.org/10.1039/C9CY00593E
[44] M. J. Antal, M. Carlsson, X. Xu, D.G.M. Anderson, Ind. Eng. Chem. Res. 37 (1998) 3820–3829. https://doi.org/10.1021/ie980204c
[45] H. Knözinger, in: S. Patal (Ed.), The Hydroxyl Group (1971), John Wiley & Sons, Ltd, 2010: pp. 641–718. https://doi.org/10.1002/9780470771259.ch12

[46] Y. Zhi, H. Shi, L. Mu, Y. Liu, D. Mei, D.M. Camaioni, J.A. Lercher, J. Am. Chem. Soc. 137 (2015) 15781–15794. https://doi.org/10.1021/jacs.5b09107
[47] O.M. Kut, R.D. Tanner, J.E. Prenosil, K. Kamholz, in: R.G. Herman (Ed.), Catalytic Conversions of Synthesis Gas and Alcohols to Chemicals, Springer US, Boston, MA, 1984: pp. 361–394.
[48] D. Mores, E. Stavitski, Marianne H. F. Kox, J. Kornatowski, U. Olsbye, B. M. Weckhuysen, Chem. Eur. J. 14 (2008) 11320 – 11327. https://doi.org/10.1002/chem.200801293
[49] D. Mores, J. Kornatowski, U. Olsbye, B. M. Weckhuysen, Chem. Eur. J. 147 (2011) 2874-2884. https://doi.org/10.1002/chem.201002624
[50] Z. Qin, K.A. Cychosz, G. Melinte, H. El Siblani, J.-P. Gilson, M. Thommes, C. Fernandez, S. Mintova, O. Ersen, V. Valtchev, J. Am. Chem. Soc. 139 (2017) 17273–17276. https://doi.org/10.1021/jacs.7b10316
[51] X. Chen, T. Todorova, A. Vimont, V. Ruaux, Z. Qin, J.-P. Gilson, V. Valtchev, Microporous Mesoporous Mater. 200 (2014) 334–342. https://doi.org/10.1016/j.micromeso.2014.07.057
[52] V. Babić, L. Tang, Z. Qin, L. Hafiz, J.-P. Gilson, V. Valtchev, Adv. Mater. Interfaces. (2020). https://doi.org/10.1002/admi.202000348
[53] N. Suárez, J. Pérez-Pariente, C. Márquez-Álvarez, M. Grande Casas, A. Mayoral, A. Moreno, Microporous Mesoporous Mater. 284 (2019) 296–303. https://doi.org/10.1016/j.micromeso.2019.04.049